Temperature-Dependent Plasmonic Response of Graphene Nanoresonators

Junhyung Kim,[⊥] Geonwoo Lee,[⊥] Sergey G. Menabde, Yong Jai Cho, Carsten Rockstuhl, and Min Seok Jang*

Cite This: *ACS Photonics* 2022, 9, 2256−2262

Read Online

ACCESS | Metrics & More | Article Recommendations | Supporting Information

ABSTRACT: Graphene plasmons have attracted enormous research interest due to their dynamic tunability and the extreme field confinement they provide. However, despite their popularity, most studies revolving around graphene plasmons have been restricted to room temperature, leaving unconsidered important tunability knob. In this work, we experimentally investigate the temperature-dependent plasmonic properties of graphene nanoresonators with varying widths on SiO_2 substrate by infrared transmission spectroscopy. As temperature drops from 300 to 100 K, the intensity of the graphene plasmon resonance peak increases up to 76%, and the amount of enhancement decreases with increasing carrier concentration and decreasing resonator width. We attribute the enhancement of graphene plasmon resonance to an additional hole doping of $\Delta p = 1.37 \times 10^{12}$ cm^{-2} associated with cooling and reduced plasmon damping due to the suppression of phonon-mediated scattering channels. Our results uncover the significance of temperature effects that can be exploited in graphene-based tunable plasmonic devices operating at low temperatures.
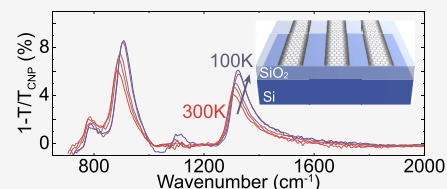
KEYWORDS: *graphene plasmons, plasmonic resonance, temperature dependence, graphene nanoresonators, low-temperature measurement*

■ INTRODUCTION

Graphene is a versatile material platform for nanophotonics and optoelectronics owing to its excellent electrical[1−3] and optical[4,5] properties that can be dynamically altered by external doping. Particularly, doped graphene exhibits a strong plasmonic response from THz to mid-infrared (mid-IR) frequencies, effectively acting as a two-dimensional metallic sheet. Such graphene sheets, possibly structured, support highly confined graphene plasmons (GP) characterized by effective wavelengths up to 2 orders of magnitude shorter than the free-space wavelength.[6−11] Therefore, graphene has been widely employed for nanophotonic applications such as active metasurfaces,[12−14] plasmonic nanoantennas,[15−17] plasmonic waveguide modulators,[18,19] and photonic crystals,[20−22] to name a few, operating at mid-IR frequencies.

Despite the growing interest in graphene plasmonics, most GP research has been performed at room temperature, and the temperature dependence of GP properties has not been widely investigated thus far.[23] A notable exception would be the study by Ni et al.[24] They examined the fundamental limits of GP damping at cryogenic temperatures through near-field imaging of propagating GPs in a high-quality exfoliated graphene encapsulated by the hexagonal boron nitride (h-BN). However, we note that practical nanophotonic devices require large-area graphene grown by chemical vapor deposition (CVD), whose quality is generally inferior to that of graphene obtained by mechanical exfoliation. Also, large-area graphene-based plasmonic devices suffer from unavoidable extrinsic loss channels originating from fabrication imperfections. The

dynamics of GP damping can also be significantly affected by the substrate material and graphene nanopatterning. Therefore, more studies on the temperature-dependent GP properties with various materials and structural combinations are urgently needed for the practical design of nanophotonic devices.

In this work, we report on the far-field investigation of the temperature-dependent mid-IR plasmonic responses of graphene nanoresonator arrays, patterned in a large-area CVD graphene film on Si/SiO$_2$ substrate. We observe that the intensities of the plasmon resonance peaks in the extinction spectra increase up to 76% as the temperature drops from 300 to 100 K. The observation can be attributed to two primary causes. First, temperature-induced hole doping of $\Delta p = 1.37 \times 10^{12}$ cm^{-2} in graphene on SiO_2 enhances the oscillator strength of graphene nanoresonators. Second, reduced plasmon damping due to the suppression of temperature-dependent scattering mechanisms prolongs the graphene plasmon lifetime, which is also evidenced by the increased quality factor of the resonances.

Both the doping concentration and the plasmon damping rate are strongly affected by the electronic properties of graphene and by the phononic properties of the SiO_2 substrate
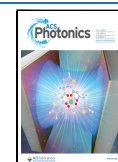
and the interface states. To decipher this intricate hybrid system and systematically verify the effects mentioned above, we conducted three independent experiments: DC electrical measurements, Raman spectroscopy, and infrared transmission spectroscopy. The cooling-induced doping effect is verified in all three measurements, and the suppressed damping is also independently supported by DC carrier mobility measurements and infrared spectroscopy. Unveiling these temperature-related effects in the graphene−SiO$_2$ system is essential for developing feasible graphene-based large-area devices operating at mid-IR frequencies.

RESULTS AND DISCUSSION

A schematic of our device—an array of graphene nanoresonators on a Si/SiO$_2$ substrate—is shown in Figure 1a. All
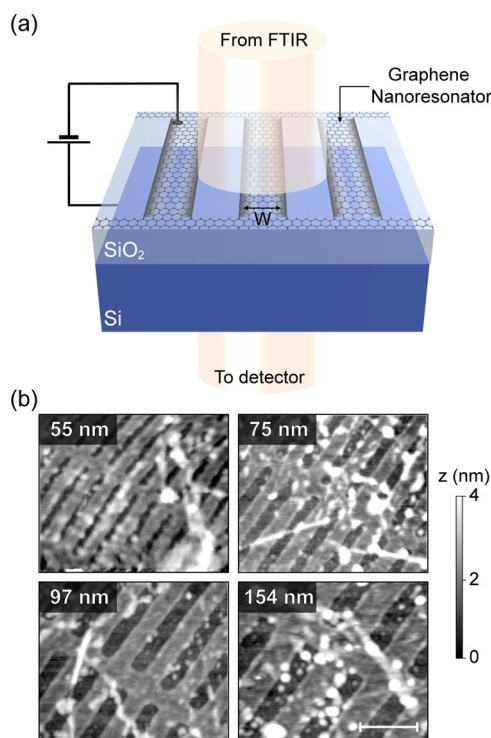
Figure 1. (a) Schematic device structure composed of graphene nanoresonators on a Si/SiO$_2$ substrate. (b) AFM images of the graphene nanoresonators with different resonator widths as noted; the scale bar is 300 nm.

devices were fabricated using graphene grown by the CVD method. To overcome the large momentum mismatch between the GP and free-space light, graphene is patterned into nanoresonators that can couple to the far field. The pattering of graphene was done by electron beam lithography followed by oxygen plasma etching. Each nanoresonator array has an area of 200 × 200 μm^2 and consists of quasi-identical nanoresonators with a fixed width W. The sample contains four arrays of graphene nanoresonators with W = 55, 75, 97, and 154 nm, measured by atomic force microscopy (AFM) after fabrication (Figure 1b).

First, to investigate the temperature dependence of the carrier concentration and the mobility of graphene, we measure the DC electrical properties of the planar graphene sheet while varying its temperature from 300 to 100 K using a nitrogen-purged heating/cooling stage. Figure 2a displays the
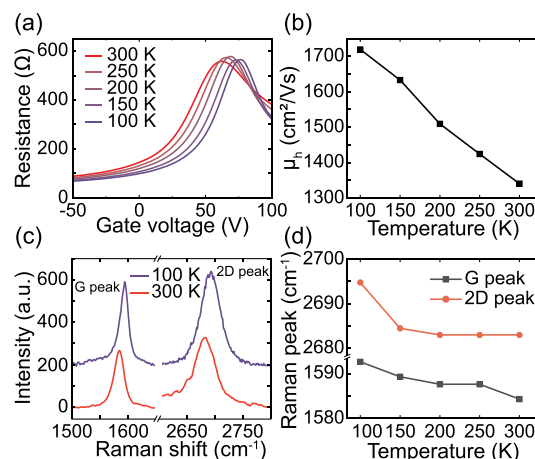
Figure 2. (a) DC resistance of planar graphene sheet as a function of the gate voltage at different temperatures. (b) Extracted hole mobility of graphene as a function of temperature. (c) Raman spectra of a single-layer CVD graphene on Si/SiO$_2$ substrate at 100 and 300 K. (d) Dependence of the spectral positions of G and 2D Raman peaks on temperature.

dependence of the device's resistance as a function of gate bias V_g measured at various temperatures. The fabricated graphene is of p type, typical for wet-transferred CVD graphene on SiO$_2$ due to water molecule during transfer process and substrate interface property. The maximum resistance point in Figure 2a, which corresponds to graphene's charge neutrality point (CNP), drifts from V_{CNP} = 62 V at 300 K to 76.5 V at 100 K. The shift of ΔV_{CNP} = 14.5 V corresponds to the additional hole concentration $\Delta p = \Delta Q/e = C\Delta V/e = \epsilon\epsilon_0\Delta V_{CNP}/ed = 1.04 \times 10^{12}$ cm^{-2}. Here, the carrier concentration can be calculated based on the parallel capacitance model, where Q is the charge density, C is the capacitance per area, and ϵ = 3.9 and d = 300 nm are the static dielectric constant and the thickness of the SiO$_2$ substrate, respectively. Constants ϵ_0 and e are the free-space permittivity and the elementary charge, respectively. Furthermore, the increased hole doping of graphene associated with cooling is observed by the blueshift of G ($\approx$1580 cm^{-1}) and 2D ($\approx$2690 cm^{-1}) Raman peaks (Figure 2c,d) that correspond to the in-plane vibrational mode of the C−C bond and the second-order two phonon processes, respectively.[25,26] A similar trend has been reported by Verhagen et al.[27] We note that this additional doping effect can be suppressed by encapsulating graphene by hexagonal boron nitride (h-BN), as demonstrated by Ni et al. in their temperature-dependent near-field measurements on propagating GP.[24] From these observations, we speculate that the additional p doping could originate from the releasing of trapped charges at the SiO$_2$−graphene interface, which may be affected by the SiO$_2$ phonons known to be rapidly extinguished at T < 200 K.[28−31] However, to the best of our knowledge, no works have yet elucidated the exact mechanism for the observed doping effect. We leave this as a subject for future investigation.

In addition to the change of doping concentration, the cooling of graphene also reduces the carrier scattering rate in graphene, leading to increased carrier mobility. By fitting the constant mobility model to the measured DC curves,[32] the temperature dependence of the hole mobility can be extracted, as shown in Figure 2b, demonstrating a monotonic increase of mobility with decreasing temperature. When analyzing the

temperature-dependent carrier mobility, which is inversely proportional to the carrier scattering rate τ^{-1}, it is instructive to consider different scattering mechanisms comprising the cumulative scattering rate given by

$$\tau_{int}^{-1} = \tau_{imp}^{-1} + \tau_{PO}^{-1} + \tau_{LA}^{-1} \tag{1}$$

Here, τ_{imp}^{-1}, τ_{PO}^{-1}, and τ_{LA}^{-1} are scattering rates due to impurities, SiO_2 polar optical phonons, and longitudinal acoustic phonons in graphene, respectively.[28,29,33] The impurity scattering rate shows little temperature dependence. On the other hand, the phonon-mediated scattering rates τ_{PO}^{-1} and τ_{LA}^{-1} rapidly decrease with cooling, while the former has a nonlinear and the latter has a linear temperature dependence. The mobility measured in our experiments shows a near-linear dependence on temperature, which agrees with the previously reported measurements at high-doping concentrations.[28,30] It is important to note that, although the carrier mobilities obtained from the DC electrical measurements provide useful insights into DC carrier dynamics of graphene, what actually determines the plasmonic response of graphene nanoribbons are the AC scattering properties at IR frequencies, which are not necessarily identical to their DC counterparts.

To characterize the plasmonic response of graphene, we measure the transmission spectra of the nanoresonator arrays using Fourier transform infrared (FT-IR) spectroscopy coupled with a computer-controlled heating/cooling stage. The excitation beam is polarized perpendicular to the nanoresonators to maximize the coupling to graphene plasmons. The temperature is varied between 300 and 100 K. We systematically investigate the temperature-dependent plasmonic properties of the graphene nanoresonators by analyzing the width-, doping-, and temperature-dependent normalized extinction spectra $1 - T_V/T_{CNP}$, where $T_V(\omega)$ is the transmission spectrum at a given gate bias, and $T_{CNP}(\omega)$ is the transmission at CNP (Figure 3). In our experiments, the maximum extinction modulation was observed to be around 10%. We note that the modulation efficiency can be dramatically improved to reach near-unity. This requires enhancing the radiative coupling rate of the system using external resonant structures.[12,34,35]

A hybrid polaritonic resonator, such as a graphene nanoresonator placed on a polar dielectric substrate, exhibits multiple resonance peaks due to the hybridization between GP and the polar phonon modes of the substrate, which has been demonstrated in previous works.[36,37] Such hybridized mode is called surface plasmon-phonon polaritons (SPPP) and manifests itself through an avoided crossing of the plasmon dispersion near the substrate phonon frequency.[8,9,38] SiO_2 has two transverse optical (TO) phonon modes at frequencies $\omega_{TO1,2} = 803.7$ and 1088 cm^{-1}, resulting in three distinctive resonances in our measured spectral range: two SPPP modes above and below ω_{TO1}, and one GP resonance above ω_{TO2} as shown in Figure 3.

Figure 3a,b illustrates how the normalized extinction spectra depend on the resonator width and carrier density, respectively, at a fixed temperature $T = 100$ K. As reported in the earlier works,[8,9] both SPPP and GP peaks blue-shift as the resonator width decreases or the carrier density increases. Once the frequency of an SPPP mode approaches the SiO_2 phonon lines ($\omega_{TO1,2}$), the SPPP peak disappears due to high phonon loss (Figure 3a). On the other hand, when the SPPP is not damped, its extinction peak intensity and that of the GP
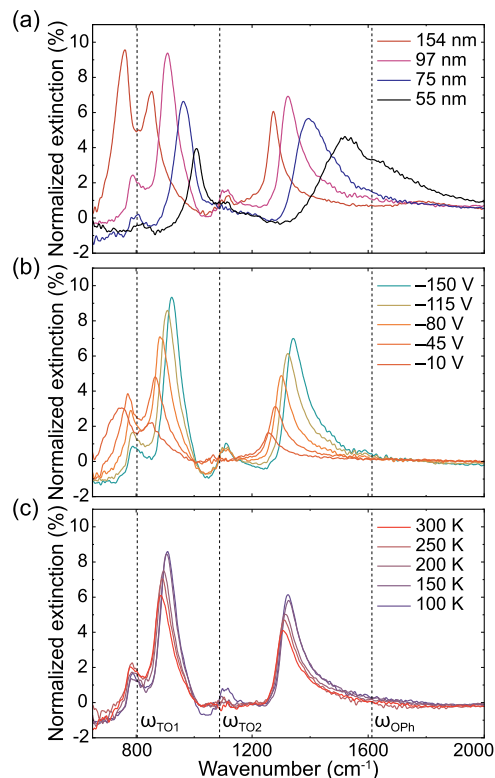
Figure 3. Normalized extinction spectra of graphene nanoresonator arrays on Si/SiO$_2$ substrate: (a) varying resonator width at fixed $V_g = -115$ V and $T = 100$ K, (b) varying V_g at fixed $W = 97$ nm and $T = 100$ K, (c) varying temperature at fixed $W = 97$ nm and $V_g = -115$ V. Vertical dashed lines indicate two transverse optical (TO) phonon modes of SiO$_2$ at frequencies $\omega_{TO1,2} = 803.7$ and 1088 cm^{-1} and graphene optical phonon at frequencies $\omega_{OPh} = 1613$ cm^{-1}.
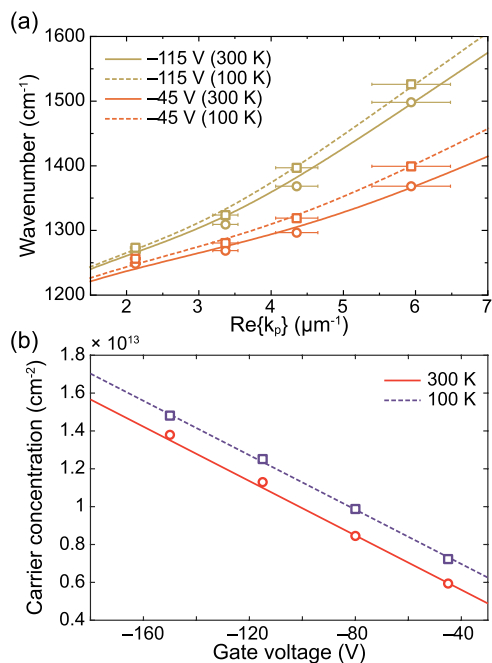
peak tend to increase with increasing doping level since the higher carrier density leads to the higher oscillator strength, as shown in Figure 3b.

Unlike the SPPP extinction profile, the GP resonance becomes spectrally broader as the nanoresonator gets narrower, as evident from Figure 3a. Since GP peaks are spectrally distant from both ω_{TO2} and ω_{OPh}, where $\omega_{OPh} = 1613$ cm^{-1} is the graphene optical phonon frequency,[39,40] the broadening of the GP peak is likely due to fabrication imperfections such as edge roughness or resonator width variation within the array. We note that the same amount of fabrication error would cause a larger peak broadening in narrower nanoresonators. To further investigate this possibility, we examined the AFM scans of the nanoresonator arrays. We found that the standard deviation of the nanoresonator width is about 5 nm for all resonators. Based on the obtained width distribution, the inhomogeneous linewidth broadening of the GP peak is estimated to be 69, 39, 20, and 2% compared to uniform nanoresonators with $W = 55$, 75, 97, and 154 nm, respectively (Supporting Information Section S1). The linewidths of SPPP peaks also depend on W and V_g. Still, in this case, it is difficult to discriminate between the intrinsic and extrinsic effects since the SPPP peak is inherently close to the SiO$_2$ phonon lines and is strongly damped.

Figure 3c shows the temperature-dependent extinction spectrum of the device with $W = 97$ nm and $V_g = -115$ V. Decreasing temperature leads to a slight blueshift and a larger intensity of all extinction peaks. This trend, which can be

explained by the increased carrier density and mobility in graphene, agrees with the electrical measurements (Figure 2a,b). We also note that additional features such as peak distortion near graphene optical phonon energy ω_{OPh} and second-order graphene plasmon peaks can be observed at low temperatures where various plasmon damping mechanisms are suppressed (see Supporting Information Section S2).

To independently estimate the doping-level variation associated with cooling apart from the aforementioned DC electrical measurement, we fit the measured peak positions (summarized in Figure S5) to the theoretical dispersion relation with the doping level as the only fitting parameter. The resulting dispersion curves agree well with the measured data (Figure 4a), which is also summarized in Figure 4b by plotting

the carrier concentration as a function of the gate bias. The optically estimated carrier densities are {1.38, 1.13, 0.85, 0.59} $\times 10^{13}$ cm^{-2} and {1.48, 1.25, 0.99, 0.72} $\times 10^{13}$ cm^{-2} at $T =$ 300 and 100 K, respectively, for $V_g = -150, -115, -80,$ and -45 V. The estimated doping levels well match the linear fit with a fixed specific capacitance of $\epsilon/d = 11.5$ nF/cm^{-2} (Figure 4b). The amount of the additional hole doping $\Delta p = 1.37 \times 10^{12}$ cm^{-2} associated with cooling from 300 K to 100 K is similar to the estimated value from the electrical measurement.

We note that the thermally induced strain in graphene cannot explain the temperature-dependent blueshift of the peak position. First, graphene has a negative thermal expansion coefficient of $-(4.8 \pm 1.0) \times 10^{-6}$ K^{-1},[41,42] and thus, cooling should induce a redshift, not a blueshift, of the resonance peak due to the expansion of the resonator width. Second, thermal expansion is only about 0.1% when temperature changes from 300 to 100 K, which is an order of magnitude smaller than the relative peak shift.

The temperature-dependent electrodynamic response of the nanoresonators can be further analyzed by extracting the intensity of the GP resonance for all measured extinction spectra at different W, V_g, and T, as shown in Figure 5. The intensity data are normalized by the maximum value at 100 K. In most cases, peak intensities increase with decreasing temperature. The peak intensity enhancement associated with cooling from 300 to 100 K ranges from 10 to 76%. We partly attribute the increasing peak intensity to the additional p doping induced by cooling, which is inferred from the similar temperature dependence of both the intensity and the position of the resonance peak (Figure S8). The temperature dependence of the peak intensity becomes stronger when the gate bias gets smaller. This is likely because the temperature-induced doping Δp becomes more significant than the electrostatically induced doping level at lower gate biases, as shown in Figure 4b.

We also compare the temperature dependence of the peak intensity for various nanoresonator sizes at the highest gate bias $V_g = -150$ V, where the effect of temperature-induced doping $\Delta p = 1.37 \times 10^{12}$ cm^{-2} becomes minimized and is about 1:10 of the electrostatically induced doping concentration. In this regime, the peak intensity variation is expected to mainly depend on the plasmon scattering rate $\tau^{-1} = \tau_{int}^{-1} + \tau_{ext}^{-1}$, where τ_{int}^{-1} and τ_{ext}^{-1} are the scattering rates associated with intrinsic and extrinsic mechanisms. τ_{int}^{-1} decreases along with temperature, as the scattering of substrate phonons and graphene acoustic phonons is suppressed. On the other hand, the extrinsic mechanisms involve plasmon scattering at the edge of the resonator, and therefore, τ_{ext}^{-1} hardly depends on temperature. Assuming that the same amount of nanoresonator
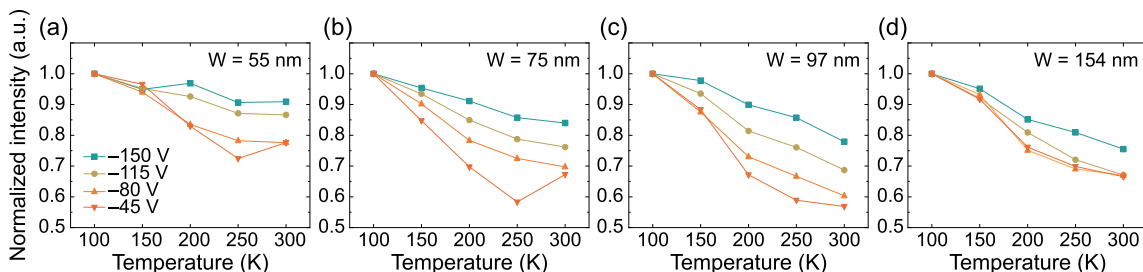

Figure 4. (a) Dispersion relation of GP at 300 K (solid) and 100 K (dashed) for $V_g = -115$ V (dark yellow) and -45 V (red). The open symbols plot the measured values, and the curves are the theoretical dispersion relations with the doping level as the only fitting parameter. The wavevector values are obtained from AFM measurements of the nanoresonator widths. The error bars indicate the inhomogeneity of the resonator width. (b) Estimated carrier concentrations from dispersion model fitting at different gate voltages are displayed as symbols. The solid lines are the linear fits assuming the constant specific capacitance $\epsilon/d = 11.5$ nF/cm^{-2}.

Figure 5. (a−d) Temperature dependence of the GP extinction peak intensities normalized by the values at $T = 100$ K. The width of the nanoresonators, W, is marked on the top right corner, and the applied gate bias values, V_g, is specified in the legend.
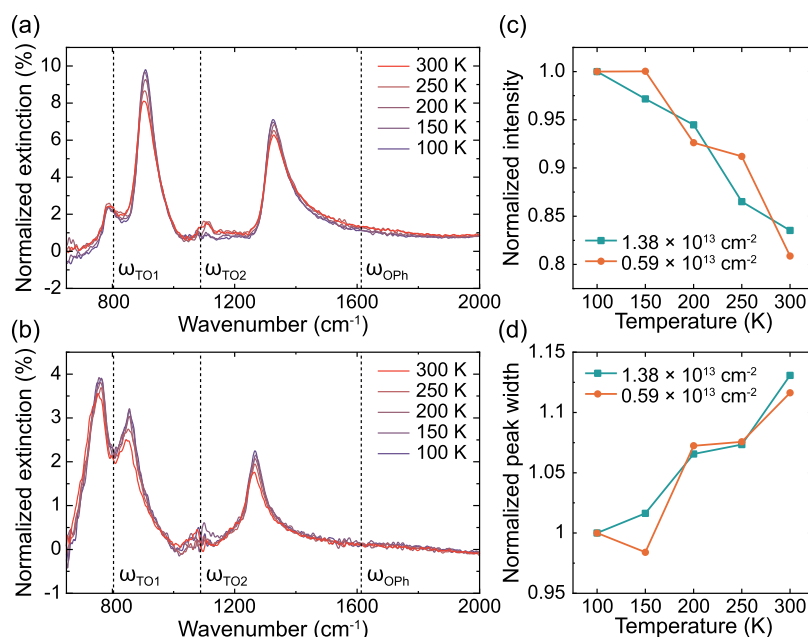
Figure 6. (a, b) Normalized extinction spectra of the GP resonance in nanoresonators with W = 97 nm at two different carrier concentrations: (a) p = 1.38 × 10^{13} cm^{-2} and (b) 0.59 × 10^{13} cm^{-2}. (c, d) Temperature dependence of the normalized intensities (c) and widths (d) of the GP resonance peaks shown in (a) and (b).

edge roughness occurs regardless of the resonator width, narrower nanoresonators are expected to have a larger contribution to the temperature-independent extrinsic scattering rate. Indeed, the normalized extinction peaks in the narrower nanoresonators are much less sensitive to temperature than those in wider nanoresonators, as shown in Supporting Information Section S8.

Finally, to eliminate the effect of the temperature-induced doping and isolate the effect of plasmon damping variation, we carried out additional measurements in which the resonance frequency of the GP peak is tuned to the same value by controlling the gate bias at each temperature in the device with W = 97 nm. We display two cases with high and low doping levels with $p \approx$ 1.38 and 0.59 × 10^{13} cm^{-2} corresponding to GP resonance frequencies of ω_{GP} = 1334 and 1269 cm^{-1}. Even after excluding the additional p-doping effect, the normalized peak intensity still increases with cooling, as shown in Figure 6c. The linewidth of the GP resonance peak, which is inversely proportional to the plasmon relaxation time, is observed to decrease with cooling, as seen in Figure 6d. Interestingly, the temperature dependences of both normalized intensity and linewidth of the GP peak show a quantitatively similar trend independent of doping level. At both p = 1.38 × 10^{13} and 0.59 × 10^{13} cm^{-2}, the peak intensity increases by ∼22%, and the linewidth decreases by ∼11% when the temperature drops from 300 to 100 K. We attribute this remnant increase in peak intensity and decrease in peak linewidth to the reduced damping of graphene plasmons. As temperature drops, the phonon-mediated carrier scattering mechanisms are suppressed.[29,43,44] Thus, the plasmon lifetime is expected to be prolonged, leading to a stronger resonance with an increased quality factor. However, it is difficult to directly extract the plasmon scattering rate from the measured peak widths since the peak width is also largely affected by other external factors, including resonator inhomogeneity within the measured area (see Supporting Information Section S1).

CONCLUSIONS

To conclude, we have analyzed the temperature-dependent plasmonic responses of graphene nanoresonators on a SiO$_2$ substrate in the far field. When the temperature drops from 300 to 100 K, the graphene plasmon resonance becomes stronger, resulting in an increase in the extinction peak intensities ranging from 10 to 76% depending on the resonator width and the applied gate bias. The increase in GP peak intensity can be attributed to the cooling-induced additional p doping and the suppression of phonon-mediated scattering mechanisms at low temperatures. Thus, our results uncover important but largely overlooked temperature effects on tunable plasmons in large-area graphene–SiO$_2$ systems, being a stepping stone toward advanced graphene plasmonic devices operating at cryogenic temperatures.

EXPERIMENTAL SECTION

The CVD graphene, prepared in the form of three layers comprising poly(methyl methacrylate) (PMMA)/CVD graphene/polymer, was purchased from Graphenea, Inc., which is ready for wet transfer procedure. The PMMA/graphene was then wet-transferred onto the Si/SiO$_2$ substrate. Electron beam evaporation was used to create the source/drain contacts of 30:50 nm thick palladium (Pd)/gold (Au). Graphene nanoresonators were patterned using 50 keV electron beam lithography on 100 nm thick 495 PMMA. The exposed PMMA was developed in a 1:3 methyl isobutyl ketone (MIBK):isopropanol solution, and the graphene was etched using oxygen plasma at an O$_2$ flow rate 10 sccm and 50 W for 3 s. Silicon in the Si/SiO$_2$ substrate was used as the back gate electrode for graphene electrostatic doping.

The current–voltage $(I–V)$ characteristics of the devices were measured semiautomatically (Keithley 2400 via a LabVIEW interface). The gate voltage was swept from −150 to 100 V, while the source–drain bias was fixed at 0.01 V. Optical characterization was performed with an FT-IR

microscope (Nicolet iS10 spectrometer and iN5 microscope, Thermo Scientific). The measurement window was set to 150 × 150 μm^2. To perform temperature-dependent measurements, the sample was placed inside the heating/cooling stage (THMS600, Linkam) during the optical characterization.

To secure similar experimental conditions among the measurements, the following steps were performed before FT-IR measurement. First, the devices were baked at 130 °C for 25 min to remove adsorbed water on the sample and further improve the transport quality of graphene.[45] After baking, the heating/cooling stage was purged with nitrogen for 3 min to replace the air inside the chamber. Each measurement took approximately 6 min to reach thermal equilibrium. The cooling stage loaded onto the FT-IR microscope was isolated from ambient air by continuous purging of nitrogen with humidity kept below 10% to prevent water condensation on the window of the stage.

■ ASSOCIATED CONTENT

ⓢ Supporting Information
The Supporting Information is available free of charge at https://pubs.acs.org/doi/10.1021/acsphotonics.1c01966.

> Calculated normalized extinction spectra of graphene nanoresonators on Si/SiO$_2$ substrate (Figure S1); normalized extinction spectra of various nanoresonator arrays at different temperatures (Figure S2); DC resistance of graphene as a function of gate voltage at different temperatures (Figure S3); estimated cooling-induced carrier concentration as a function of temperature (Figure S4); transmission spectra of bare Si/SiO$_2$ substrate at various temperatures (Figure S5); comparison between the experimental and numerically calculated extinction spectra of the GP resonance in nanoresonators (Figure S6); extracted DC and AC hole mobility of graphene as a function of temperature (Figure S7); temperature dependence of the GP peak frequency shift (Figure S8); normalized intensities of the GP extinction peak as a function of temperature (Figure S9); estimated GP peak intensities of inhomogeneous resonators normalized by those of uniform resonators (Table S1); and estimated GP linewidths of inhomogeneous resonators normalized by those of uniform resonators (Table S2) (PDF)

■ AUTHOR INFORMATION

Corresponding Author
Min Seok Jang − *School of Electrical Engineering, Korea Advanced Institute of Science and Technology, Daejeon 34141, Republic of Korea;* ◉ orcid.org/0000-0002-5683-1925; Email: jang.minseok@kaist.ac.kr

Authors
Junhyung Kim − *School of Electrical Engineering, Korea Advanced Institute of Science and Technology, Daejeon 34141, Republic of Korea*
Geonwoo Lee − *School of Electrical Engineering, Korea Advanced Institute of Science and Technology, Daejeon 34141, Republic of Korea*
Sergey G. Menabde − *School of Electrical Engineering, Korea Advanced Institute of Science and Technology, Daejeon 34141, Republic of Korea;* ◉ orcid.org/0000-0001-9188-8719

Yong Jai Cho − *Advanced Instrumentation Institute, Korea Research Institute of Standards and Science, Daejeon 34113, Republic of Korea*
Carsten Rockstuhl − *Institute of Theoretical Solid State Physics, Karlsruhe Institute of Technology, 76131 Karlsruhe, Germany; Institute of Nanotechnology, Karlsruhe Institute of Technology, 76021 Karlsruhe, Germany*

Complete contact information is available at:
https://pubs.acs.org/10.1021/acsphotonics.1c01966

Author Contributions
[⊥]J.K. and G.L. contributed equally to this work. J.K., G.L., and M.S.J. conceived the idea. J.K. and G.L. fabricated the samples. G.L. performed the temperature-dependent measurements. Y.J.C. measured the optical properties of the substrate. J.K., G.L., S.G.M., and M.S.J. analyzed the experimental data. J.K., S.G.M., C.R., and M.S.J. wrote the manuscript. M.S.J. supervised the project.

Notes
The authors declare no competing financial interest.

■ ABBREVIATIONS
IR, infrared; GP, graphene plasmons; CVD, chemical vapor deposition; DC, direct current; AFM, atomic force microscopy; CNP, charge neutrality point; FT-IR, Fourier transform infrared; SPPP, surface plasmon-phonon polaritons; TO, transverse optical

■ REFERENCES
(1) Novoselov, K. S.; Geim, A. K.; Morozov, S. V.; Jiang, D.; Zhang, Y.; Dubonos, S. V.; Grigorieva, I. V.; Firsov, A. A. Electric field effect in atomically thin carbon films. *Science* **2004**, *306*, 666−669.
(2) Neto, A. H. C.; Guinea, F.; Peres, N. M. R.; Novoselov, K. S.; Geim, A. K. The electronic properties of graphene. *Rev. Mod. Phys.* **2009**, *81*, 109−162.
(3) Hwang, E. H.; Sarma, S. D. Screening-induced temperature-dependent transport in two-dimensional graphene. *Phys. Rev. B* **2009**, *79*, No. 165404.
(4) Avouris, P. Graphene: Electronic and Photonic Properties and Devices. *Nano Lett.* **2010**, *10*, 4285−4294.
(5) Bonaccorso, F.; Sun, Z.; Hasan, T.; Ferrari, A. C. Graphene photonics and optoelectronics. *Nat. Photonics* **2010**, *4*, 611−622.
(6) Hwang, E. H.; Sarma, S. D. Dielectric function, screening, and plasmons in two-dimensional graphene. *Phys. Rev. B* **2007**, *75*, No. 205418.
(7) Jablan, M.; Buljan, H.; Soljacic, M. Plasmonics in graphene at infrared frequencies. *Phys. Rev. B* **2009**, *80*, No. 245435.
(8) Yan, H. G.; Low, T.; Zhu, W. J.; Wu, Y. Q.; Freitag, M.; Li, X. S.; Guinea, F.; Avouris, P.; Xia, F. N. Damping pathways of mid-infrared plasmons in graphene nanostructures. *Nat. Photonics* **2013**, *7*, 394−399.
(9) Brar, V. W.; Jang, M. S.; Sherrott, M.; Lopez, J. J.; Atwater, H. A. Highly Confined Tunable Mid-Infrared Plasmonics in Graphene Nanoresonators. *Nano Lett.* **2013**, *13*, 2541−2547.
(10) Kim, S.; Menabde, S. G.; Brar, V. W.; Jang, M. S. Functional Mid-Infrared Polaritonics in van der Waals Crystals. *Adv. Opt. Mater.* **2020**, *8*, No. 1901194.
(11) Grigorenko, A. N.; Polini, M.; Novoselov, K. S. Graphene plasmonics. *Nat. Photonics* **2012**, *6*, 749−758.

(12) Kim, S.; Jang, M. S.; Brar, V. W.; Mauser, K. W.; Kim, L.; Atwater, H. A. Electronically Tunable Perfect Absorption in Graphene. *Nano Lett.* **2018**, *18*, 971−979.

(13) Han, S.; Kim, S.; Kim, S.; Low, T.; Brar, V. W.; Jang, M. S. Complete Complex Amplitude Modulation with Electronically Tunable Graphene Plasmonic Metamolecules. *ACS Nano* **2020**, *14*, 1166−1175.

(14) Hu, H.; Yang, X. X.; Zhai, F.; Hu, D. B.; Liu, R. N.; Liu, K. H.; Sun, Z. P.; Dai, Q. Far-field nanoscale infrared spectroscopy of vibrational fingerprints of molecules with graphene plasmons. *Nat. Commun.* **2016**, *7*, No. 12334.

(15) Fang, Z. Y.; Liu, Z.; Wang, Y. M.; Ajayan, P. M.; Nordlander, P.; Halas, N. J. Graphene-Antenna Sandwich Photodetector. *Nano Lett.* **2012**, *12*, 3808−3813.

(16) Jornet, J. M.; Akyildiz, I. F. Graphene-based Plasmonic Nano-Antenna for Terahertz Band Communication in Nanonetworks. *IEEE J. Sel. Areas Commun.* **2013**, *31*, 685−694.

(17) Llatser, I.; Kremers, C.; Cabellos-Aparicio, A.; Jornet, J. M.; Alarcon, E.; Chigrin, D. N. Graphene-based nano-patch antenna for terahertz radiation. *Photonic Nanostruct. - Fundam. Appl.* **2012**, *10*, 353−358.

(18) Jang, M. S.; Kim, S.; Brar, V. W.; Menabde, S. G.; Atwater, H. A. Modulated Resonant Transmission of Graphene Plasmons Across a lambda/50 Plasmonic Waveguide Gap. *Phys. Rev. Appl.* **2018**, *10*, No. 054053.

(19) Kim, S.; Menabde, S. G.; Cox, J. D.; Low, T.; Jang, M. S. Ultracompact electro-optic waveguide modulator based on a graphene-covered lambda/1000 plasmonic nanogap. *Opt. Express* **2021**, *29*, 13852−13863.

(20) Chen, K.; Zhou, X.; Cheng, X.; Qiao, R. X.; Cheng, Y.; Liu, C.; Xie, Y. D.; Yu, W. T.; Yao, F. R.; Sun, Z. P.; Wang, F.; Liu, K. H.; Liu, Z. F. Graphene photonic crystal fibre with strong and tunable light-matter interaction. *Nat. Photonics* **2019**, *13*, 754−759.

(21) Liu, J. T.; Liu, N. H.; Li, J.; Li, X. J.; Huang, J. H. Enhanced absorption of graphene with one-dimensional photonic crystal. *Appl. Phys. Lett.* **2012**, *101*, No. 052104.

(22) Majumdar, A.; Kim, J.; Vuckovic, J.; Wang, F. Electrical Control of Silicon Photonic Crystal Cavity by Graphene. *Nano Lett.* **2013**, *13*, 515−518.

(23) Xing, Q. X.; Song, C. Y.; Wang, C.; Xie, Y. G.; Huang, S. Y.; Wang, F. J.; Lei, Y. C.; Yuan, X.; Zhang, C.; Mu, L.; Huang, Y.; Xiu, F. X.; Yan, H. G. Tunable Terahertz Plasmons in Graphite Thin Films. *Phys. Rev. Lett.* **2021**, *126*, No. 147401.

(24) Ni, G. X.; McLeod, A. S.; Sun, Z.; Wang, L.; Xiong, L.; Post, K. W.; Sunku, S. S.; Jiang, B. Y.; Hone, J.; Dean, C. R.; Fogler, M. M.; Basov, D. N. Fundamental limits to graphene plasmonics. *Nature* **2018**, *557*, 530−533.

(25) Ferrari, A. C. Raman spectroscopy of graphene and graphite: Disorder, electron-phonon coupling, doping and nonadiabatic effects. *Solid State Commun.* **2007**, *143*, 47−57.

(26) Ferrari, A. C.; Meyer, J. C.; Scardaci, V.; Casiraghi, C.; Lazzeri, M.; Mauri, F.; Piscanec, S.; Jiang, D.; Novoselov, K. S.; Roth, S.; Geim, A. K. Raman spectrum of graphene and graphene layers. *Phys. Rev. Lett.* **2006**, *97*, No. 187401.

(27) Verhagen, T. G. A.; Drogowska, K.; Kalbac, M.; Vejpravova, J. Temperature-induced strain and doping in monolayer and bilayer isotopically labeled graphene. *Phys. Rev. B* **2015**, *92*, No. 125437.

(28) Chen, J. H.; Jang, C.; Xiao, S. D.; Ishigami, M.; Fuhrer, M. S. Intrinsic and extrinsic performance limits of graphene devices on SiO2. *Nat. Nanotechnol.* **2008**, *3*, 206−209.

(29) Chen, J. H.; Jang, C.; Ishigami, M.; Xiao, S.; Cullen, W. G.; Williams, E. D.; Fuhrer, M. S. Diffusive charge transport in graphene on SiO2. *Solid State Commun.* **2009**, *149*, 1080−1086.

(30) Balasubramanian, K.; Chandrasekar, H.; Raghavan, S. Carrier Transport in Graphene Field-Effect Transistors on Gated Polar Nitride Substrates. *Phys. Status Solidi A* **2020**, *217*, No. 1900949.

(31) Fratini, S.; Guinea, F. Substrate-limited electron dynamics in graphene. *Phys. Rev. B* **2008**, *77*, No. 195415.

(32) Kim, S.; Nah, J.; Jo, I.; Shahrjerdi, D.; Colombo, L.; Yao, Z.; Tutuc, E.; Banerjee, S. K. Realization of a high mobility dual-gated graphene field-effect transistor with Al2O3 dielectric. *Appl. Phys. Lett.* **2009**, *94*, No. 062107.

(33) Heo, J.; Chung, H. J.; Lee, S. H.; et al. Non-monotonic temperature dependent transport in graphene grown by Chemical Vapor Deposition. *Phys. Rev. B* **2011**, *84*, No. 035421.

(34) Jang, M. S.; Brar, V. W.; Sherrott, M. C.; Lopez, J. J.; Kim, L.; Kim, S.; Choi, M.; Atwater, H. A. Tunable large resonant absorption in a midinfrared graphene Salisbury screen. *Phys. Rev. B* **2014**, *90*, No. 165409.

(35) Kim, S.; Jang, M. S.; Brar, V. W.; Tolstova, Y.; Mauser, K. W.; Atwater, H. A. Electronically tunable extraordinary optical transmission in graphene plasmonic ribbons coupled to subwavelength metallic slit arrays. *Nat. Commun.* **2016**, *7*, No. 12323.

(36) Liu, Y.; Willis, R. F. Plasmon-phonon strongly coupled mode in epitaxial graphene. *Phys. Rev. B* **2010**, *81*, No. 081406.

(37) Koch, R. J.; Seyller, T.; Schaefer, J. A. Strong phonon-plasmon coupled modes in the graphene/silicon carbide heterosystem. *Phys. Rev. B* **2010**, *82*, No. 201413.

(38) Brar, V. W.; Jang, M. S.; Sherrott, M.; Kim, S.; Lopez, J. J.; Kim, L. B.; Choi, M.; Atwater, H. Hybrid Surface-Phonon-Plasmon Polariton Modes in Graphene/Monolayer h-BN Heterostructures. *Nano Lett.* **2014**, *14*, 3876−3880.

(39) Nika, D. L.; Balandin, A. A. Two-dimensional phonon transport in graphene. *J. Phys. Condens. Matter* **2012**, *24*, No. 233203.

(40) Falkovsky, L. A. Symmetry constraints on phonon dispersion in graphene. *Phys. Lett. A* **2008**, *372*, 5189−5192.

(41) Mounet, N.; Marzari, N. First-principles determination of the structural, vibrational and thermodynamic properties of diamond, graphite, and derivatives. *Phys. Rev. B* **2005**, *71*, No. 205214.

(42) Yoon, D.; Son, Y. W.; Cheong, H. Negative Thermal Expansion Coefficient of Graphene Measured by Raman Spectroscopy. *Nano Lett.* **2011**, *11*, 3227−3231.

(43) Hwang, E. H.; Das Sarma, S. Acoustic phonon scattering limited carrier mobility in two-dimensional extrinsic graphene. *Phys. Rev. B* **2008**, *77*, No. 115449.

(44) Zhu, W. J.; Perebeinos, V.; Freitag, M.; Avouris, P. Carrier scattering, mobilities, and electrostatic potential in monolayer, bilayer, and trilayer graphene. *Phys. Rev. B* **2009**, *80*, No. 235402.

(45) Cheng, Z. G.; Zhou, Q. Y.; Wang, C. X.; Li, Q. A.; Wang, C.; Fang, Y. Toward Intrinsic Graphene Surfaces: A Systematic Study on Thermal Annealing and Wet-Chemical Treatment of SiO2-Supported Graphene Devices. *Nano Lett.* **2011**, *11*, 767−771.